Bistatic Synthetic Aperture Target Detection and Imaging With an AUV

Joseph R. Edwards, Henrik Schmidt, and Kevin D. LePage

Abstract—The acoustic detection and classification of completely and partially buried objects in the multipath environment of the coastal ocean presents a major challenge to the mine countermeasures (MCM) community. However, the rapidly emerging autonomous underwater vehicle (AUV) technology provides the opportunity of exploring entirely new sonar concepts based on mono-, bi- or multi-static configurations. For example, the medium frequency regime (1–10 kHz) with its bottom penetration advantage may be explored using large synthetic apertures, where acoustic information is accumulated over a series of sonar pings. The performance of such approaches is highly dependent on accurate platform navigation and timing, which poses a significant challenge to AUV developers, particularly because the navigation procedures are themselves dependent on the complicated multipath acoustic environment. Data from the GOATS'98 experiment have been analyzed to investigate the feasibility of combining seabed scattering data from consecutive pings of a fixed parametric source to form a bistatic synthetic aperture for target localization and imaging with an AUV based receiving platform. The paper describes different levels of bistatic processing including both incoherent and coherent beamforming and very large aperture interferometric approaches, and the associated performance tradeoffs are discussed.

Index Terms—Autonomous underwater vehicles, bistatic, buried targets, mine countermeasures, synthetic aperture sonar.
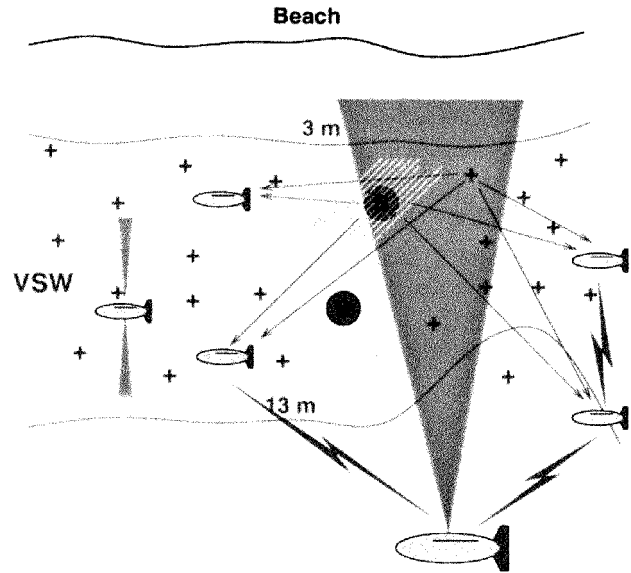
Fig. 1. GOATS concept for concurrent detection and classification of seabed targets using a network of AUVs for forming a multistatic synthetic aperture. The master vehicle is insonifying the seabed from off-shore, connected with the receiver vehicle network using a high-bandwidth communication and navigation network. The multistatic synthetic aperture processing is applied for detection while the mapping of the 3-D scattered field is used for classification.

I. INTRODUCTION

A high coverage rate is desirable for operational mine countermeasures (MCM) detection and classification. In shallow and very shallow water (VSW), mines can be either proud, buried, or partially buried, depending on the environmental conditions. Classical MCM sonar systems operate at a high frequency, typically 30+ kHz, to provide a resolution adequate for the acoustic imaging that is the basis for target classification. Except for a few pathological cases, the environmental acoustics does not allow these sonars to detect targets completely buried in the seabed at standoff ranges beyond critical, which for typical seabeds amounts to a few times the sonar altitude. This in turn severely limits the coverage rate of such systems against buried mines.

The generic ocean array technology sonar (GOATS) concept uses a fleet of small autonomous underwater vehicles (AUVs) cooperating in a volumetric mapping of the acoustic scattering from proud or buried targets. It is specifically aimed

at expanding the coverage rate for shallow and VSW MCM by performing concurrent detection and classification of proud and buried targets, exploring the unique three-dimensional (3-D) spatial and temporal features of low- to mid-frequency target scattering. A potential application of GOATS is illustrated in Fig. 1. One AUV insonifies the VSW seabed from off-shore with a powerful mid-frequency source such as a parametric sonar. The scattered field is measured by a formation of small AUVs equipped with acoustic arrays. The data are preprocessed and transmitted via a high-bandwidth communication capability to the master vehicle where the data from the multiple receiver platforms are combined to create a seabed image, as well as a 3-D map of the target scattering, which then forms the basis for both detection and classification.

There are several fundamental scientific and applied technology issues that must be resolved before the MCM performance of the GOATS concept can be evaluated. Among these unresolved issues are characterization of the mid-frequency (1–10 kHz) insonification regime, extension of sonar processing techniques to bi-static and multi-static scenarios, and optimization of information processing for the robust detection and classification of man-made objects. The use of the mid-frequency regime is of necessity for adequate bottom penetration [1], but it also provides additional information
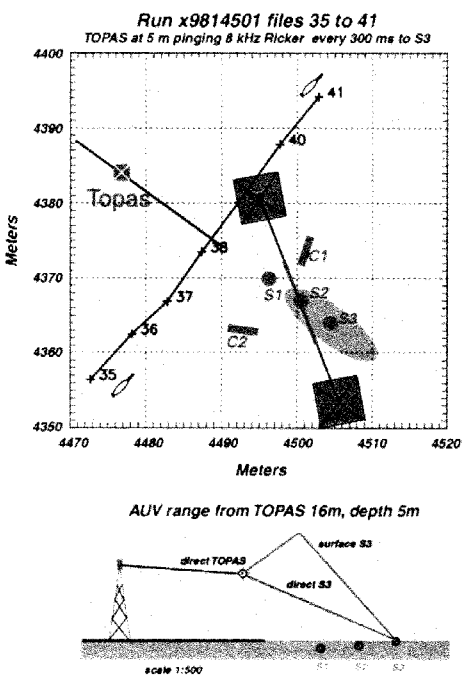
Fig. 2. GOATS'98 experimental geometry. A TOPAS parametric source is mounted on a tower which may be relocated along a horizontal rail to change angles of incidence on the seabed targets. A fixed 128-element horizontal hydrophone array was suspended 5 m over the targets for fixed bistatic measurements, while an AUV equipped with a receiving array and acquisition system was used as a moving receiver platform, creating synthetic apertures at different offsets from the target field.
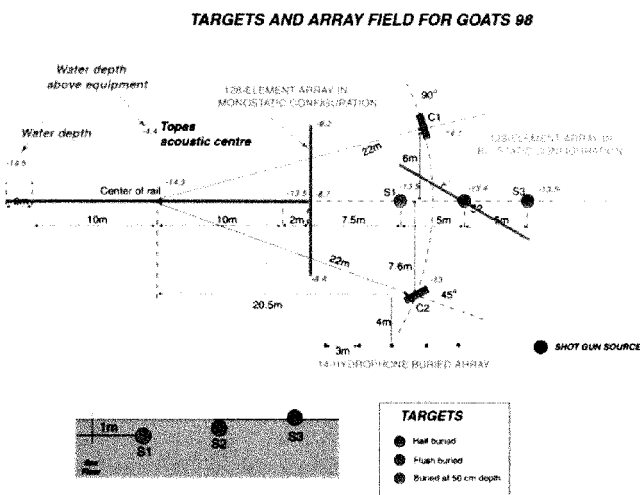

Fig. 3. Layout of the target field for GOATS'98. Five targets were deployed, three empty spherical shells, half-buried (S3), flush-buried (S2), and completely buried (S1), respectively. In addition, two water-filled cylindrical shells were flush buried, at aspects of 90° (C1), and 45° (C2), respectively. The targets were deployed such that they could be insonified at angles above and below the critical grazing angle of approximately 24° [7]. Here the horizontal line array is shown in a quasi-monostatic configuration.

for classification by exciting frequency-dependent responses of the target. Bi- and multi-static scenarios complicate the data processing significantly, but they also increase the survey coverage rate and provide additional target information by measuring aspect-dependent responses of the target. Both of these results can be regarded as forms of data diversity, which may be used as an aid in cases where traditional high-frequency monostatic imaging fails. In sonar applications, there has been relatively little study of alternative techniques for buried target classification, although some laboratory-based studies have shown promise [2]–[4]. Data diversity techniques have been effectively employed in the buried landmine case [5], [6], where, as in the underwater case, the imaging wavelength is on the order of the target size.

This paper details some early findings from this research project, based on data acquired with an AUV-borne acoustic acquisition system in the GOATS'98 experiment. This experiment was carried out at Marciana Marina, Elba Island, in May 1998 to investigate various aspects of the GOATS concept, including fundamental seabed penetration physics, use of seismic sources, and navigation and control performance for AUVs in VSW.

II. GOATS'98 BISTATIC IMAGING EXPERIMENT

During the bistatic imaging phase of the GOATS'98 experiment, a stationary source was used to insonify a patch on the seafloor that contained a known target field (Fig. 2). The source used was a topographic parametric sonar (TOPAS), which provides a highly directive beam on a given patch of the seafloor.

A receiver array mounted on an AUV was used to sample the scattered field. The experiment was performed in an area close to shore with a water depth of 14 m and a sandy seabed. The sound velocity profile of the water column was a nearly uniform 1520 m/s.

A. Source

The TOPAS sonar is a parametric source with a secondary frequency band of 2–16 kHz. The source level in the secondary frequency band is 201 dβ re μPa @ m. This relatively low frequency band was chosen for improved seabed penetration, which in turn enhances the buried target detection capability. Although reduction in frequency obviously increases penetration at super-critical angles, the more interesting regime for rapid mapping is subcritical insonification, which has been shown to provide significant evanescent wave field penetration in this frequency range [7]. The source transmitted a series of pings at a repetition period of 300 ms, with each ping being a broad-band Ricker wavelet with a center frequency of 8 kHz.

As illustrated in Fig. 2, the parametric projector was mounted on a 10-m-tall tower that could be repositioned along a 20-m-long rail on the seabed to allow target insonification at grazing angles below as well as above the critical angle of approximately 24° for penetration into the seabed [7]. During the experiment, both sub- and super-critical insonification angles were tested, but the current work concerns only subcritical grazing angles.

B. Target Field

Five targets of various geometry and burial conditions were deployed in a relatively smooth portion of sandy seabed, in an area 10–20 m from the end of the TOPAS rail, as shown in Fig. 3. The targets included three air-filled spherical steel shells with a diameter of 1 m and a wall thickness of 3 cm. One was half-buried (S3), one flush-buried (S2), and one was buried 0.9
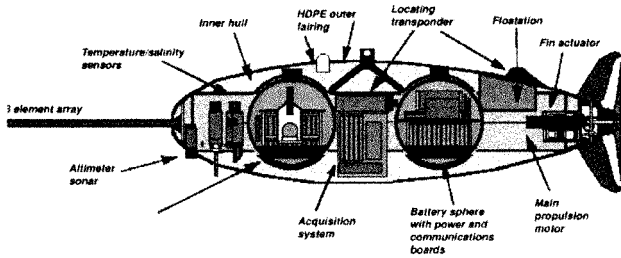
MIT Odyssey configuration for GOATS 98

Fig. 4. Odyssey II AUV equipped with an 8-element array in a "swordfish" configuration. The element spacing is 10 cm. A dedicated acquisition system is mounted in the center bay of the vehicle, with data stored on disk for post-processing.
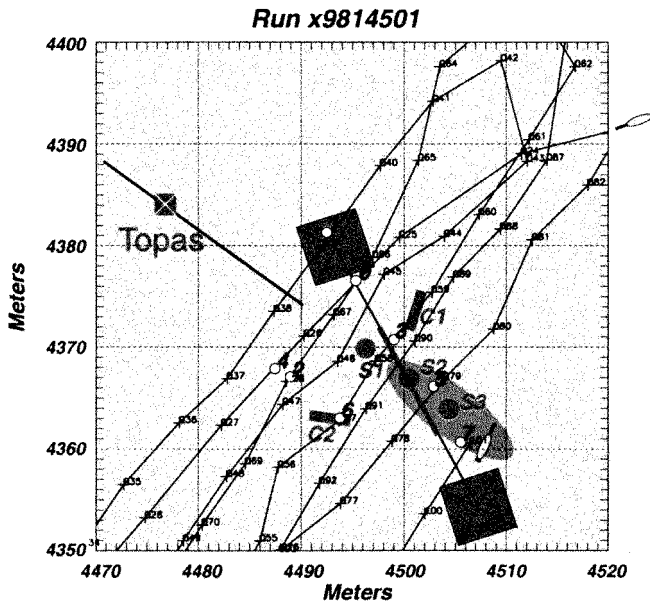
Run x9814501

Fig. 5. AUV track over the target field.

m below the surface (S1) at its center. In addition, two steel cylinders were flush-buried at aspect angles of 90° (C1) and 45° (C2), respectively. The 2-m-long and 50-cm-diameter cylinders were both water-filled and had a shell thickness of 6 mm.

C. Autonomous Underwater Vehicle

The AUV used as a receiver platform was an Odyssey II AUV equipped with a linear acoustic array in a "swordfish" configuration, as can be seen in Fig. 4. The array consisted of eight omnidirectional hydrophones linearly spaced with $\Delta x = 0.1$ m, which corresponds to the $\lambda/2$ sampling at 7.5 kHz. The apparent undersampling is mitigated by the fact that the array is not required to steer over the full 180 degree half-space.

The AUV was programmed to perform a "lawn-mower" survey over the target field, with the actual AUV track indicated by the lines crossing the target field in Fig. 5. The AUV was navigated using an 8–12-kHz-long baseline (LBL) acoustic navigation system to travel between way-points alternating between the two sides of the target field. It used the LBL to update its position and adjust the trajectory every 10 s. The numbers on the AUV track indicate the vehicle position

when the LBL navigation cycle was initiated. The navigation cycle was interleaved with the TOPAS transmissions to avoid mutual interference. To synchronize the transmissions with the navigation cycle, the LBL interrogation pulse was detected by the TOPAS receiver electronics, triggering a 7-s ping sequence after a 3-s delay. Thus, only 7 s of data were available for SAS processing in each navigation cycle, corresponding to a 7-m synthetic aperture.

III. Theory

In a littoral environment, the returns from a given source include the direct return and several types of correlated multipath returns. Highly correlated multipath returns can be used coherently to improve detection and classification capability. The sea surface, however, cannot generally be assumed to be stable enough for consistent highly correlated multipath returns. A further consequence of working in shallow water is increased reverberation noise. The low frequencies required for seabed penetration serve to increase the reverberation time. This effect limits the pulse repetition rate of the sonar to a lower rate than would otherwise be possible at such short range.

A. Signal Characterization

In this study, a simple linear system model is used to represent the signal path. Thus, the received signal is modeled in the time domain as a convolution of the input signal with a series of filters, including the medium impulse response, the target response, and the transmitter and receiver beampatterns. In the monostatic case, an echo return can then be written as [8]

$$e_i(t) = \sum_{j=1}^{J} s(t) * h(t, \tau_{ij}) * a_j(t, \theta_{ij}) * b_{\mathrm{p}}(t, \theta_{ij}) * b_h(t, \theta_{ij}) \quad (1)$$

where $s(t)$ is the source signal, $h(t, \tau_{ij})$ is the impulse response of the time-invariant medium, $a_j(t, \theta_{ij})$ is the impulse response of scatterer j, $b_{\mathrm{p}}(t, \theta_{ij})$ is the level of the projector beampattern in the direction of scatterer j, and $b_h(t, \theta_{ij})$ is the level of the receiver beampattern in the direction of scatterer j.

In the GOATS'98 scenario, the receiver is not at the source position, and the bistatic response of the target must therefore be considered. Analysis of the resulting signal return is greatly complicated by this fact. The source angle remains the same, but there is now a receiver angle that is not in the same plane as the receiver in general. With these considerations, the linear system model of the received signal then becomes

$$e_i(t) = \sum_{j=1}^{J} s(t) * h(t, \tau_{ij}) * a_j\left(t, \theta_{ij}^{(r)}, \phi_{ij}^{(r)}; \theta_{ij}^{(s)}\right)$$
$$* b_{\mathrm{p}}\left(t, \theta_{ij}^{(s)}\right) * b_h\left(t, \theta_{ij}^{(r)}\right) \quad (2)$$

where the superscripts (r) and (s) correspond to the receiver and the source, respectively.

For imaging purposes, the echo return will be assumed to be the result of a simple environmental model that includes only a direct and a surface-reflected return from each scatterer. Within this model, several assumptions will be applied, as listed below.

- Only the scatterers in the main lobe of the projector contribute, i.e., $b_{\mathrm{p}}\left(t, \theta_{ij}^{(r)}\right) \approx 1$.
- The scatterers do not fluctuate with time, due to the stationary projector.
- The sea surface behaves as a pressure-release plane boundary.
- The bistatic scattering strengths of the direct and surface-reflected returns are approximately equal for each scatterer.

These assumptions can be used to recast the echo return model into the following form:

$$
\begin{aligned}
e_i(t) \approx s(t) \sum_{j=1}^{J} & \frac{\mu_j\left(\theta_{ij}^{(r)}, \phi_{ij}^{(r)}; \theta_{ij}^{(s)}\right)}{r_{ij}^{(p-t)}\left(\theta_{ij}^{(s)}\right)} \\
& * \left\{\frac{\delta\left(t - \tau_{ij}^{\mathrm{dir}}\right)}{r_{ij}^{(t-r)}\left(\theta_{ij}^{(r)}, \phi_{ij}^{(r)}\right)} - \frac{\delta\left(t - \tau_{ij}^{\mathrm{SR}}\right)}{r_{ij}^{(t-s)} r_{ij}^{(s-r)}}\right\}
\end{aligned}
\tag{3}
$$

where μ_j is the scattering strength of scatterer j, τ_{ij}^{dir} and τ_{ij}^{SR} indicate the time delays of the direct and surface-reflected returns, and the projector to target scatterer, target scatterer to receiver, target scatterer to sea surface, and sea surface to receiver straight line distances are indicated by $r_{ij}^{(p-t)}$, $r_{ij}^{(t-r)}$, $r_{ij}^{(t-s)}$, and $r_{ij}^{(s-r)}$, respectively.

From this point, the generation of the image data is straightforward. Given the receiver position i, the receiver is focused on a patch centered on the desired scatterer j. The receiver beampattern is then approximately unity in the region of the scatterer. The scattering coefficient is then extracted by a matched filtering process, using the environmental model to form the matching filter. This extraction is implemented as an inner product between the measured signal and the return replica $R(t)$:

$$
\mu_j\left(\theta_{ij}^{(r)}, \phi_{ij}^{(r)}; \theta_{ij}^{(s)}\right) \approx R_j^H(t) e_i(t).
\tag{4}
$$

Finally, if the array aperture spans an angular region over which the bistatic scattering strength is nearly constant, the result is equivalent to the canonical monostatic image, except that the image is evaluated at some fixed bistatic angle.

B. Vehicle Navigation

Navigation of the AUVs is perhaps the most critical limiting factor for precise imaging in the GOATS scenario. There are two methods of navigation used by the AUV, which can be classified by scale. The *global* navigation is performed by AUVs using a variety of systems, such as inertial navigation systems (INS), Doppler-Velocity Logs (DVL), or an acoustic system such as the LBL system used in GOATS'98, all in combination with GPS while surfaced. The *local* navigation is accomplished by a self-navigation process based on the acoustic data, and both methods come into play in the processing decision.

The global fix navigation is the more straightforward consideration of the two. Between the 7-s acoustic acquisition periods, the LBL network provides a global position estimate with estimated error bounds. However, the current technology, and likely the technology for some time to come, does not allow a global position estimate accuracy on the order of the acoustic wavelength needed for acoustic array processing. Consequently, the use of LBL navigation is limited to anchoring the image in space, and coherent processing based on global navigation alone is not considered here.

The local navigation, often termed "micro-navigation," provides a much finer position estimate. However, the micro-navigation provides only relative positions, and as such the positional uncertainty increases with time. It is clear that the error will, at some point, reach a level such that coherent processing can no longer be implemented in a robust manner. In this case, it makes sense to micro-navigate until the error reaches the order of the LBL network, thus maximizing the amount of acoustic data, and then initiate an LBL cycle. The full micro-navigated array can then be segmented into coherent parts.

Sonar self-navigation techniques generally rely on the coherence (or lack thereof) of the return from the insonified patch, and fall into two categories: *target*-based and *reverberation*-based navigation. Target-based navigation relies on the availability of a strong, well-placed target (or targets) and large, high-resolution apertures. Neither of these requirements are in place for general AUV applications.

Reverberation-based navigation instead relies on having a large number of independent scatterers of roughly equal magnitude to generate a signal return that is nearly uncorrelated in space. The self-navigation technique used in the current work is based on the displaced phase center antenna (DPCA) approach commonly used for monostatic synthetic aperture sonar (SAS). This method has been shown to compensate for positional errors and array calibration errors simultaneously [9].

1) The DPCA Method: In the traditional DPCA approach, the displaced phase centers of the quasimonostatic array are located midway between the source and receiver. Each displaced phase center behaves as a single purely monostatic source/receiver element. If the platform, which includes source and receiver in the monostatic case, moves less than 1/2 of the physical receiver aperture length between ping receptions, then there will be overlap between the received signals. This region of overlap is then used to determine the trajectory of the vehicle to subwavelength accuracy.

For general bistatic sonar, the displaced phase center approach is invalid, because the displaced phase center cannot be considered a single purely monostatic source/receiver element. The representation of the displaced phase centers as monostatic elements arises from Crispin's monostatic to bistatic equivalence theorem (MBET) approximation, which states [10] that the bistatic scattering cross section σ_{B} is the monostatic scattering cross section σ_{M} evaluated at half the bistatic look angle β, i.e.,

$$
\sigma_{\mathrm{B}}(\theta, f) = \sigma_{\mathrm{M}}\left(\theta = \frac{\beta}{2}, f\right).
\tag{5}
$$

This theorem is valid for simple objects with a bistatic look angle (β) less than $10°$, which may be violated by general bistatic sonar.

However, with restricted source motion, the technique is easily extended. With the stationary source in the GOATS'98

experiment, the *actual* receiver positions can be used in the place of the displaced phase centers. An overlap in the physical receiver aperture corresponds to an overlap in the data. The platform velocity can then be as high as a full physical receiver aperture length between ping receptions. With this modification, the along-track motion estimate is the same as in the monostatic case. Cross-track motions will vary from the monostatic case, as they will generally be functions of the bistatic reflection and the receiver angle.

2) Along-Track Micro-Navigation: The simplest micro-navigation method is the estimation of platform velocity. Its original formulation was for the purpose of estimation of ship speed [11]. The nominal platform velocity $v_{p,nom}$ and the pulse repetition period τ_{PRP} are chosen such that there is significant overlap of the physical receiver aperture between consecutive receptions. Then the sensors at which there is a maximum correlation between the reverberation returns indicate the platform velocity. For a linear array, we can write

$$v_p \approx \frac{\Delta x}{\tau_{PRP}} \qquad (6)$$

where Δx corresponds to the distance along the physical array between the sensors with maximum correlation across the consecutive pings. This estimate can be considered a 1-D navigation, as it estimates only the along-track translation of the sonar platform.

3) Cross-Track Micro-Navigation: Cross-track micro-navigation encompasses the remaining two dimensions of platform motion, including translation and rotation in both planes. Most common micro-navigation methods in SAS imaging restrict the motion estimate to the slant-range plane, referring to the projected translations and rotations as sway and yaw, respectively. Theoretical studies have have shown that effective 2-D micro-navigation with the DPCA method requires phase difference estimation within a small fraction of the characteristic wavelength [12]. In particular, the fact that the yaw estimate is dependent on the individual sway estimates causes a high error variance, and a bias in the resulting micro-navigation. Despite this high sensitivity, the 2-D micro-navigation technique has been proven effective in at-sea experiments with towfish [13].

Sway estimation can normally be extracted from the velocity estimate with minimal computational cost. In the monostatic case, it is simply the time lag of the maximum correlation coefficient between consecutive pings multiplied by the medium wave speed. The hardware at the time of the GOATS'98 experiment did not provide a reliable source trigger synchronization with the data acquisition system, so the sway estimate was not possible.

C. The Bistatic Effect

Classical imaging is optimized for detection, and it averages out any frequency or angular diversity in the data [8]. Monostatic SAS will generally provide a better imaging performance, but this property is not useful in cases where the image resolution is insufficient for classification. Detection without classification results in unacceptably high false alarm rates in sonar mine hunting applications.
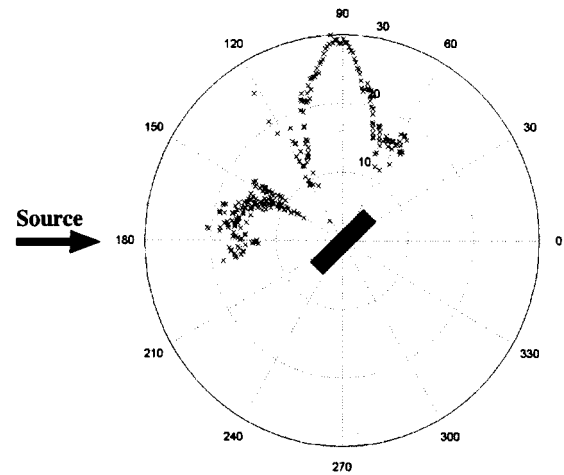

Fig. 6. Scattered field of the flush-buried cylinder measured by the HLA. The backscattered signal is 10–15 dβ less than that scattered near 90°. The distinctive shape of the scattered field can also be used as a clue for classification.

The bistatic nature of the GOATS geometry is in some ways inconsistent with the concept of imaging. Bistatic measurements are spread over a range of bistatic angles, and as such the removal of the propagation effects leaves a scattering strength that is a function of receiver position, i.e., the image is created using an inconsistent basis. However, it is precisely this property that may give the bi- and multi-static configurations their potential for concurrent detection and classification. The SAS platform motion techniques remain very important to preserve coherence of the bistatic data, but alternative processing techniques are required to preserve the data diversity that is critical for classification.

Spectral and angular diversity for classification purposes have not yet been fully exploited, but the preliminary analysis provides evidence that each of these and their combination can provide important classification clues. For example, a fixed horizonal line array (HLA) was also used in the GOATS'98 experiment to measure the scattered field from the targets. The strongly aspect-dependent field of the cylinder C2 under subcritical insonification, as measured by the HLA, is shown in Fig. 6. Such aspect-dependence provides a basis for interest in bistatic classification.

D. Coherent and Incoherent SAS

For the maximization of the signal-to-noise ratio (SNR) and resolution of the synthetic aperture, coherent processing is obviously desirable. Incoherent signal processing is generally only used when environmental parameters disallow confidence in coherent processing. In the GOATS scenario, there are several reasons that a reduction in SNR and resolution may be accepted in favor of an incoherent approach. However, coherent processing should be used as much as possible while maintaining a robust and computationally efficient system. Accuracy, simplicity and robustness must all be considered in the AUV application. With these in mind, some of the significant factors contributing to the coherent vs. incoherent processing decision are outlined in this section.
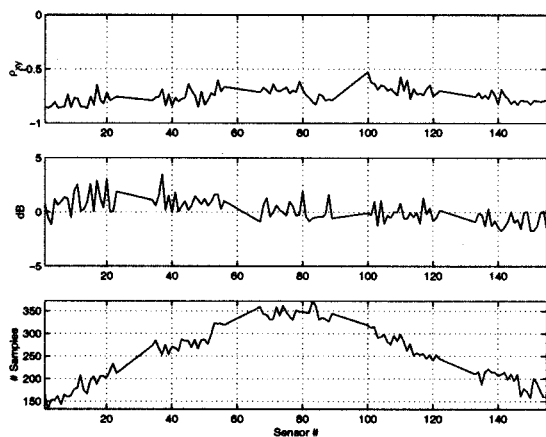
Fig. 7. Relationship between the surface reflected return and the direct return from S3, pass 23–27. The pass limits correspond to the numbers in Fig. 5. The upper frame is the correlation coefficient, the center frame is the decibel difference in the peak amplitudes, and the lower frame is the lag (in samples) between the returns.

In considering buried or elastic targets (or in this case both), there will be returns that are delayed or advanced relative to the assumed straight ray propagation through a water medium. These returns will tend to sum out as noise in near-field processing. However, they also contain information about a relevant target, so eliminating them through beamforming will result in a loss of information useful for both detection and classification. This information loss could be inconsequential if the target is easily detectable, or it could be extremely significant, as in cases where the direct return either does not exist or is masked by a stronger scatterer. Incorporating an unknown seabed and unknown elastic returns coherently would require iterating over possible medium properties, as in matched field processing [14], or over the depth dimension, as in seismic migration [15]. An incoherent approach may allow robust imaging over the medium with small changes in the propagation paths, caused either by elastic delays or medium sound velocity changes. Coherent processing begins to degrade detection capability of delayed returns once the aperture reaches a length at which range information cannot be ignored. As such, a likely choice would be to limit the coherent processing to plane-wave beamforming.

Several other sources of received signal incoherence have not been investigated in this work. Temporal and spatial nonstationarity effects are neglected, as the VSW waveguide is assumed to be well mixed and the ranges involved are very short, on the order of 10 m. The loss of coherence due to the cumulative micro-navigation error is not quantitatively considered due to hardware limitations at the time of the experiment, although it may be of significant magnitude.

IV. GOATS'98 SYNTHETIC APERTURE PROCESSING

A. Surface Reflection Coherence

In a multipath environment, it is often possible to use known coherent returns as an imaging aid. In the GOATS'98 scenario, multipath arrivals resulting from the sea surface reflection are known to exist, but the extent to which they are coherent with the direct arrivals is unknown. The most simplistic model of the sea surface is as a flat pressure-release boundary that reflects
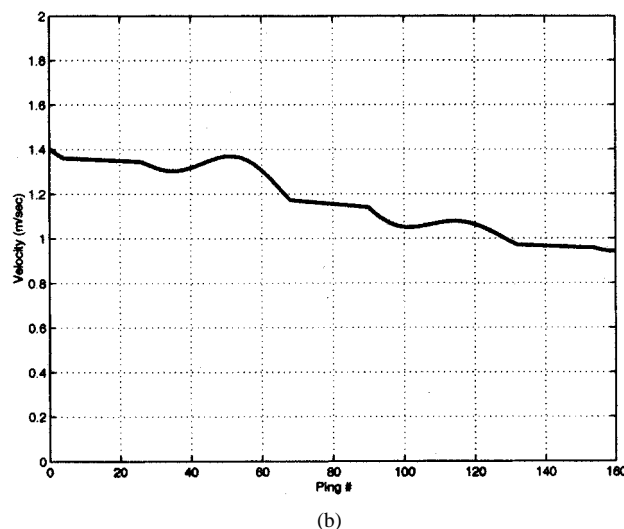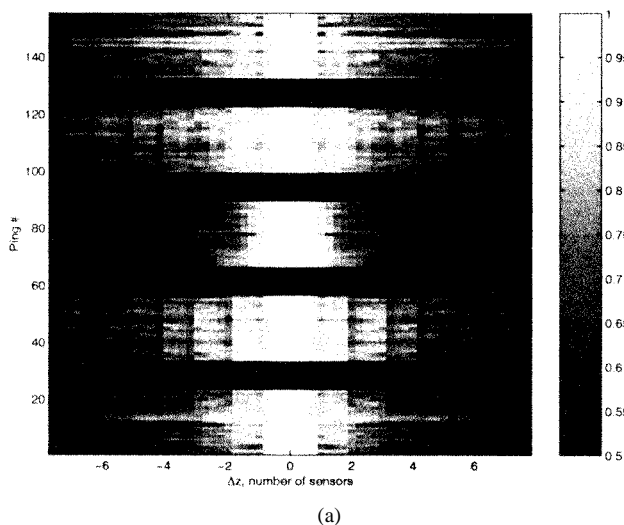

(a)

(b)

Fig. 8. (a) Maximum correlation coefficient between the patch returns measured by sensors on the physical aperture, pass 23–27. The blank sections are during the LBL cycle. (b) The corresponding vehicle velocity estimate.

the incident wave 180° out of phase. However, waves and other disturbances at the ocean surface will cause a degradation in the coherence and arrival time of the surface-reflected returns. It is therefore useful to investigate the coherence of the surface-reflected returns to determine whether they can be used in a coherent or incoherent processor. Otherwise, these returns become strictly noise.

Fig. 7 illustrates the stability of the surface-reflected return from the half-buried sphere during one full pass of the AUV, which includes 115 pings over 50 s. The upper frame a shows the correlation coefficient between the direct and the surface-reflected returns. The correlation is consistently around -0.7, a fairly high magnitude, and the sign is as expected for a pressure-release boundary. The center frame shows the peak sound pressure difference between the two returns. The two are consistently within 3 dB of each other, which indicates that the assumptions made about the bistatic return will be valid. It is not surprising that the bistatic angle between the returns does not have a significant impact on the reflection coefficient for the spherical target. The lower frame shows the time difference between the two returns (in samples). This difference appears to
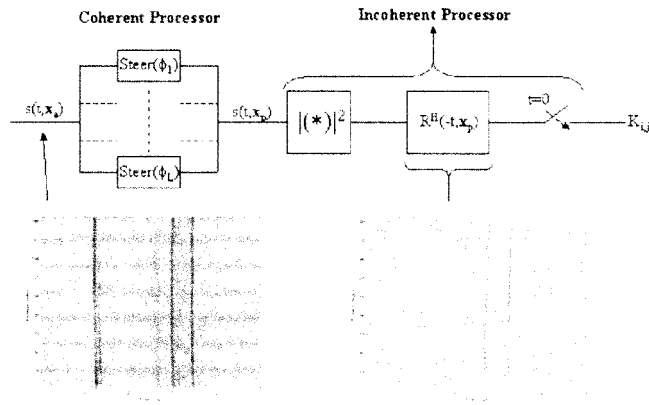
Fig. 9. Schematic diagram of the image generation algorithm. The aligned synthetic aperture data $s(t, \vec{x}_a)$ are split into spatial blocks. The data in each block are then coherently focused on the current pixel (i, j). The output of the coherent processor, $s(t, \vec{x}_\mathrm{p})$, is the collection of the steered time series, one for each coherent block. This output is then passed to an incoherent matched filtering process. The matched filter, $R^H(-t, \vec{x}_\mathrm{p})$, is the expected direct reflection plus surface bounce from the current pixel. The output of the incoherent processor is the image intensity at the given pixel, $K_{i,j}$.

Fig. 10. Extremes of the imaging process, file 25. The SAS extends from the origin to $x \approx 6.7$ m along the x axis. (a) Fully incoherent image. (b) Fully incoherent image with the half-buried sphere time-gated out. (c) Fully coherent image. (d) Fully coherent image with the half-buried sphere time-gated out.

be fairly smooth, in spite of the fact that the time of arrival of the surface reflection is very sensitive to several uncertain parameters, such as the proximity of the AUV, source and target, the uncertainty in the receiver position, and the bistatic nature of the problem. The oscillation of the times of arrival corresponds to a peak to peak wave height of only 35 cm, but this is enough to preclude coherent inclusion of the surface-reflected return without more advanced processing techniques than are presented here.

B. Patch Coherence and Vehicle Navigation

The coherence of the insonified patch returns can be seen as a measurement of the radiated power spectrum at a given angle [16]. The angle of arrival can affect the ability of the AUV to navigate based on the patch returns. For example, if the patch is at end-fire, the signals arriving on the AUV array will be nearly perfectly correlated. The AUV maintains a receiving angle with the patch within a range of $\pm 60°$ to avoid this problem. The maximum correlation coefficient between patch returns on the physical aperture is shown in the upper frame of Fig. 8, for the same pass as in the above section. The patch correlation coefficients show that the returns are correlated significantly over 2 to 3 sensor spacings, corresponding to a seabed correlation length of approximately 40 cm [17].

The lower frame shows the vehicle velocity estimate for the same pass of the target field, calculated with (6). The nominal AUV velocity is 1 m/s, and it can be seen that the velocity estimate indicates that the vehicle was slowing from a higher speed down to the nominal velocity. This was in fact the case, as this pass is the first pass of the run, and the AUV was slowing from its approach speed down to its mapping speed.

C. Target Detection and Imaging

The data were first aligned using a linear motion assumption, i.e., using the 1-D micro-navigation technique described above. This process resulted in a straight linear synthetic array. Due to
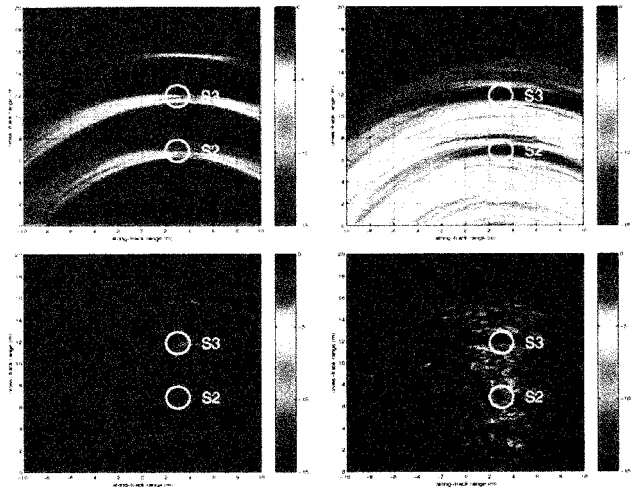
hardware limitations in the GOATS'98 experiment, the time of the source trigger then had to be determined by a least squares fit of the hyperbolic return times of a known strong scatterer in the data.

Once the synthetic aperture data is assimilated and aligned, the imaging process is an inversion to calculate the reflection coefficient at a given pixel j. The general form of the algorithm that is used for the GOATS'98 data is shown schematically in Fig. 9. The aligned synthetic aperture data at all sensor positions $\vec{x}_a$ are divided spatially into blocks that are passed into a coherent processor or beamformer. The coherent processor effectively reduces the number of elements to be passed through the incoherent processor by replacing each block with a single beamformed response at each block phase center, which are located at points $\vec{x}_\mathrm{p}$. The squared amplitude of the output of the coherent processor is then passed through an incoherent matched filter, where the matched filter for receiver element i is denoted as $R_{ij}(t)$ and is derived from the signal model in (3), i.e.,

$$
R_{ij}(t) = \left| \frac{s(t)}{r_{ij}^{(p-t)}\left(\theta_{ij}^{(s)}\right)} * \left\{ \frac{\delta\left(t - \tau_{ij}^{\mathrm{dir}}\right)}{r_{ij}^{(t-r)}\left(\theta_{ij}^{(r)}, \phi_{ij}^{(r)}\right)} - \frac{\delta\left(t - \tau_{ij}^{\mathrm{SR}}\right)}{r_{ij}^{(t-s)} r_{ij}^{(s-r)}} \right\} \right|
$$

(7)

where the time delays and ranges are calculated for each position $\vec{x}_\mathrm{p}$. The result of the imaging algorithm will in general be an average of the reflection coefficient over the range of bistatic angles included in the synthetic aperture. For a consistent basis of comparison, all images shown are from a single 7-s data file, which includes 23 pings. The file corresponds to the line from '25' to '26' in Fig. 5. The insonification grazing angle is subcritical (18.7°) and the receiver grazing angle is supercritical (35°).

1) Incoherent and Coherent SAS Imaging: One extreme of the imaging algorithm is to bypass the coherent processing block altogether and incoherently sum all of the channels in the

synthetic aperture. The image value at pixel j can be expressed in this case as

$$K_j = \sum_{n=0}^{N-1} R_{nj}^H(t) \left| e_n(t) \right|^2 \qquad (8)$$

where N is the number of elements in the SAS, R_{nj} is the signal replica for element n, and $e_n(t)$ is the measured echo return at element n. In this case, a signal replica is produced for each element and the matched filter outputs are summed incoherently.

The use of the surface-reflected multipath return in the incoherent processing generates image side-lobes of -3 dβ, which can allow a strong scatterer to mask other targets. Due to the circular ambiguity of each sensor, a very long aperture is needed to localize a target. This method was applied to the 7-m synthetic aperture, and the resulting image can be seen in upper left of Fig. 10.

In this figure, it can be seen that the half-buried sphere is clearly detected. However, the sphere image has two significant side-lobes in range, one of which masks the image of the flush-buried sphere, S2. This is a major limitation of the incoherent matched filter approach. The simplest, although not necessarily the most robust, way around this is to simply remove bright scatterers from the data. The upper right image is created by time-gating to remove the returns from S3. Once S3 is removed from the data, S2 can be seen in the image much more clearly than it can be seen in the physical aperture data, although it appears to be located further from the receiver than expected.

The lower images show the other extreme in the imaging algorithm, which is to use all of the information possible for coherent imaging. In this case, the image value at pixel j is given by

$$K_j = R_{0j}^H(t) \left| \sum_{n=0}^{N-1} e_n(t - \tau_{nj}) \right|^2 \qquad (9)$$

where R_{0j} is the signal replica at the SAS phase center, N is the total number of elements in the SAS, and τ_{nj} is the time delay of the return on element n from pixel j relative to the return at the phase center. In this case, echoes are delayed by the proper amount to focus on the given pixel, and then the inner product is taken with a single incoherent matched filter at the SAS phase center to extract the image value. The coherent processing is performed in time domain due to the broadband nature of the signal.

The synthesized array then is focused in range and azimuth, so the accuracy of the data alignment becomes more important. The inclusion of range information causes returns that do not fit the standard imaging model to destructively interfere, as is illustrated in the images. The return from the buried target, S2, appears to be a mode of the sphere, which is delayed and therefore not properly focused in the image. The direct return is not apparent, and in fact may not exist due to the evanescent insonification. Although the target can still be seen in the image, the detection capability is slightly degraded by focused coherent processing. While fully coherent processing would seem to be the optimal way to extract the most information from the SAS,
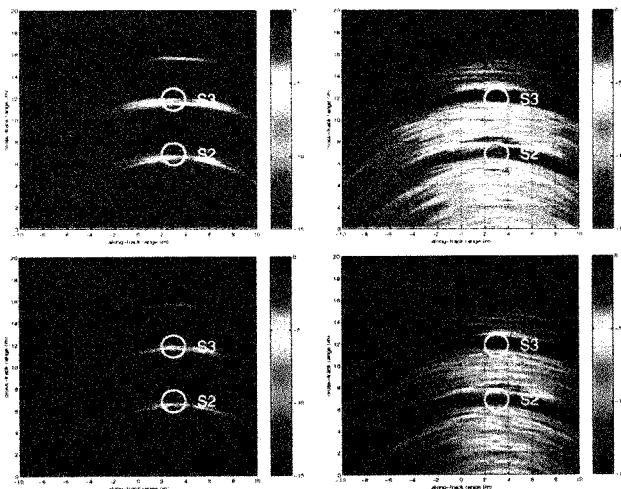

Fig. 11. Balancing coherent and incoherent processing, run 25. The SAS extends from the origin to $x \approx 6.7$ m along the x axis. (a) Plane wave beamforming on the physical apertures. (b) The same as (a), with S3 time-gated out. (c) Plane wave beamforming on 5-ping apertures. (d) The same as (c), with S3 time-gated out.

it is more sensitive to geometrical or data alignment uncertainties than is incoherent processing.

2) Coherent–Incoherent SAS Compromise: In the case of the GOATS'98 dataset, there is no way to know the cumulative navigation error along the synthetic aperture, due to the hardware limitations mentioned previously. In future work, the navigation error will be quantifiable, and it will be possible to balance the micro-navigation error with the length of coherent aperture. Here, the length of the synthetic aperture segment for coherent processing is chosen based on other concerns. With the mixed processing, the image value at pixel j is given by

$$K_j = \sum_{m=0}^{M-1} R_{mj}^H(t) \left| \sum_{n=0}^{N_m-1} e_n(t - \tau_{nj}) \right|^2 \qquad (10)$$

where M is the number of coherent processing blocks and N_m is the number of elements in block m. The elements within the coherent block are delayed and summed to focus on the given pixel, and then the inner product is taken with a matched filter evaluated at the phase center of the block. This process is repeated for the M blocks, and the results are summed incoherently. The block length can be decided based on the desired balance between coherent and incoherent processing.

The most obvious balance to be applied is to coherently process the receptions along the physical aperture, since the relative sensor position error is small and known. The physical aperture can be steered toward each pixel, then the steered physical aperture returns can be summed incoherently with the multipath arrival. This process minimizes the effect of the micro-navigation error. The images created with this method are shown in the upper half of Fig. 11. These images show that the angular resolution is significantly improved, and the buried target is slightly more readily detectable.

Although the cross-track motion in the current data set is unknown, the micro-navigation proved to be fairly accurate based on the coherent imaging results. Because of the apparent accuracy in the synthesized array positions, it is not necessary to

limit the coherent processing to only the physical array. Another reasonable balance can be met by choosing the aperture length such that it is maximized within the constraint that plane-wave beamforming can be applied. The maximum length of the array with this criterion is about 2.4 m or a 5-ping aperture. Using exclusively plane wave processing reduces the computation requirement and eliminates the problem of defocusing returns that arrive later or earlier than expected. This choice of aperture results in the images shown in the lower half of the figure. In this case, both of the insonified targets can be seen. The incoherent matched-filtering side-lobes remain a problem, but this method appears to be optimal for creating an accurate image.

V. CONCLUSION

Bistatic imaging for detection and localization of buried and elastic targets with the use of an AUV platform has been investigated. First, the data coherence and ability of the AUV to self-navigate were demonstrated, highlighting the abilities and limitations of the current technology. The self-navigation capability and data coherence establish the AUV as a viable bistatic imaging platform. Several image generation methods were employed and evaluated on their merits with the view of robust and computationally efficient applications to the AUV. The primary competing criteria for synthetic aperture length were found to be resolution and focusing. The aperture should be as long as possible to maximize resolution, but focusing effects accentuate mismatch on returns from elastic and buried targets. It was found that a balance of maximizing the length of the array while maintaining plane wave processing provided the best imaging results and minimized information loss.

REFERENCES

[1] H. Schmidt and J. Lee, "Physics of 3-d scattering from rippled seabeds and buried targets in shallow water," *J. Acoust. Soc. Amer.*, vol. 105, no. 3, pp. 1605–17, 1999.

[2] D. Boulinguez and A. Quinquis, "Underwater buried object recognition using wavelet packets and Fourier descriptors," in *Proc. 10th Int. Conf. on Image Analysis and Processing*, Los Alamitos, CA, 1999, pp. 478–83.

[3] H. L. Roitblat, W. W. L. Au, P. E. Nachtigall, R. Shizumura, and G. Moons, "Sonar recognition of targets embedded in sediment," *Neural Networks*, vol. 8, no. 7-8, pp. 1263–73, 1995.

[4] H. J. Simpson, B. H. Houston, C. K. Frederickson, and R. Lim, "Measurements and analysis of scattering from proud and buried targets in a shallow-water laboratory environment," in *Proc. MTS/IEEE Oceans'99 Conf. : Riding the Crest into the 21st Century*, vol. 3, Piscataway, NJ, 1999, pp. 1154–7.

[5] K. O'Neill, "Broadband bistatic coherent and incoherent detection of buried objects beneath randomly rough surfaces," *IEEE Trans. Geosci. Remote Sensing*, vol. 38, no. 2, pp. 891–8, Mar. 2000.

[6] W. R. Scott Jr, J. S. Martin, and G. D. Larson, "Investigation of a technique that uses elastic waves to detect buried land mines," in *Proc. IEEE 2000 Int. Geoscience and Remote Sensing Symp.*, vol. 4, Piscataway, NJ, 2000, pp. 1640–2.

[7] A. Maguer, W. L. J. Fox, H. Schmidt, E. Pouliquen, and E. Bovio, "Mechanisms for subcritical penetration into a sandy bottom: Experimental and modeling results," *J. Acoust. Soc. Amer.*, vol. 107, no. 3, 2000.

[8] M. P. Hayes and P. T. Gough, "Broad-band synthetic aperture sonar," *IEEE J. Oceanic Eng.*, vol. 17, pp. 80–94, Jan. 1992.

[9] A. Bellettini, S. Fioravanti, and M. Pinto, "Preliminary Experimental Investigation of Synthetic Aperture Sonar Micronavigation," NATO SACLANT Undersea Research Centre, La Spezia, Italy, Tech. Rep, 1999.

[10] R. L. Eigel Jr and A. J. Terzouli Jr, "Bistatic scattering characterization of a complex object," in *Proc. IEEE Int. Symp. Antennas and Propagation Soc.*, vol. 3, Dec. 1999, pp. 1784–7.

[11] P. N. Denbigh, "A design study for a correlation log to measure speed at sea," *J. Navigation*, vol. 35, pp. 160–184, 1982.

[12] M. Pinto, S. Fioravanti, and E. Bovio, "Accuracy of Synthetic Aperture Sonar Micronavigation Using a Displaced Phase Center Antenna," NATO SACLANT Undersea Research Centre, La Spezia, Italy, Tech. Rep, 1998.

[13] M. A. Pinto, A. Bellettini, S. Fioravanti, S. Chapman, D. R. Bugler, Y. Perrot, and A. Hetet, "Experimental investigations into high resolution sonar systems," in *Proc. MTS/IEEE Oceans'99 Conf. : Riding the Crest into the 21st Century*, vol. 2, Piscataway, NJ, 1999, pp. 916–22.

[14] A. B. Baggeroer, W. A. Kuperman, and H. Schmidt, "Matched field processing: Source localization in correlated noise as an optimum parameter estimation problem," *J. Acoust. Soc. Amer.*, vol. 83, no. 2, Feb. 1988.

[15] R. Stolt, "Migration by Fourier transform," *Geophys.*, vol. 43, no. 1, 1978.

[16] V. V. Ol'Shevskii, *Characteristics of Sea Reverberation*. New York: Consultants Bureau, 1967.

[17] D. Tang, "Acoustic Wave Scattering From a Random Ocean Bottom," Ph.D., MIT/WHOI, Cambridge, MA, 1991.

Joseph R. Edwards was born in Buffalo, NY, in 1971. He received the B.S.M.E. and M.S.M.E. degrees from Virginia Polytechnic Institute and State University, Blacksburg, in 1994 and 1996, respectively. He is currently working toward the Ph.D. degree in ocean engineering at the Massachusetts Institute of Technology, Cambridge.

From 1996 to 1999, he was an Acoustic Engineer for the Engineering Technology Center in Mystic, CT. His research interests are in signal and information processing and acoustics, particularly as applied to multi-platform detection and classification of buried targets.

Henrik Schmidt was born in Denmark in 1950. He received the M.S. degree in civil engineering and the Ph.D. degree in experimental mechanics from the Technical University of Denmark in 1974 and 1978, respectively.

Holding positions of Research Fellow from 1978 to 1980 at the Technical University of Denmark, and from 1980 to 1982 at Risoe National Laboratory, Denmark, he worked on numerical modeling of wave propagation and scattering phenomena in relation to nondestructive testing of structures. From 1982 to 1987, he was Scientist and Senior Scientist at SACLANT Undersea Research Centre, La Spezia, Italy, where he developed the SAFARI code for modeling seismo-acoustic propagation in ocean waveguides. In 1987, he joined the Massachusetts Institute of Technology, Cambridge, where he is currently Professor and Associate Head of Ocean Engineering. His primary research interest is the interaction of underwater sound with seismic waves in the seabed and the Arctic ice cover. Other interests include computational acoustics and matched field processing, and the use of acoustics in autonomous oceanographic sampling networks.

Prof. Schmidt is a fellow of the Acoustical Society of America and a member of the Society of Exploration Geophysicists.

Kevin D. LePage was born in East Lansing, MI, in 1961. He received the B.S. degree from Webb Institute in 1983 and the S.M. and Ph.D. degrees in ocean engineering from the Massachusetts Institute of Technology, Cambridge, in 1986 and 1992, respectively.

From 1983 to 1987, he was a Naval Architect at DTNSRDC in Cabin John, MD, where he developed conceptual designs for naval combatants. From 1992 to 1997, he was Scientist and later Senior Scientist at BBN, Cambridge, MA, where he worked on problems related to propagation and scattering in the Arctic, hydroacoustic detection of nuclear detonations, active noise and vibration control, and structural acoustics. Since 1997, he has been Senior Scientist at SACLANTCEN, La Spezia, Italy, where his primary responsibility has been the development of acoustic models for the prediction of scattering and reverberation in shallow and very shallow water at low-to-mid frequencies.